ORIGINAL ARTICLE

lajss.org
Latin American Journal of Solids and Structures

www.lajss.org

Mechanical Properties of Random Honeycomb Material under Compression-shear Combined Loading

Yiyao Gui[a], Yaozhi Xiao[a], Feng Hu[a], Ziyuan Li[a], Chengpeng Chai[a], Geng Luo[a*], Yisong Chen[a*]

[a] School of Automobile, Chang'an University, Xi'an, 710064, China. Email: guiyiyao@chd.edu.cn, 2017902359@chd.edu.cn, 2025222036@chd.edu.cn, 2025222057@chd.edu.cn, chaicp@chd.edu.cn, luogeng@chd.edu.cn, chenyisong_1988@chd.edu.cn

* Corresponding author

https://doi.org/10.1590/1679-7825/e9148

Abstract

To further analyze the mechanical properties of random porous materials under combined loading, this paper constructs a series of random honeycomb models based on Voronoi diagrams and 3D printing. A compression-shear combined loading fixture was designed. Experiments on random honeycomb materials were conducted through the universal testing machine and the proposed fixture. The results show that reducing the cell size decreases both normal and shear stresses when relative density is consistent, while increasing the loading angle increases shear stress and decreases normal stress. Furthermore, to explore the dynamic mechanical properties, the finite element model is established. The results show that random honeycomb materials exhibit three deformation modes: random mode, transitional mode, and impact mode. Then, the sensitivity analysis of the loading angles and velocities on the yield stress is carried out. The normal stress is mainly affected by the loading velocities, and both the loading angles and velocities have significant effect on the shear stress. Finally, a phenomenological yielding criterion is established.

Keywords

Mechanics; Random honeycomb; Shear-compression combined loading; Yield criterion

Graphical Abstract

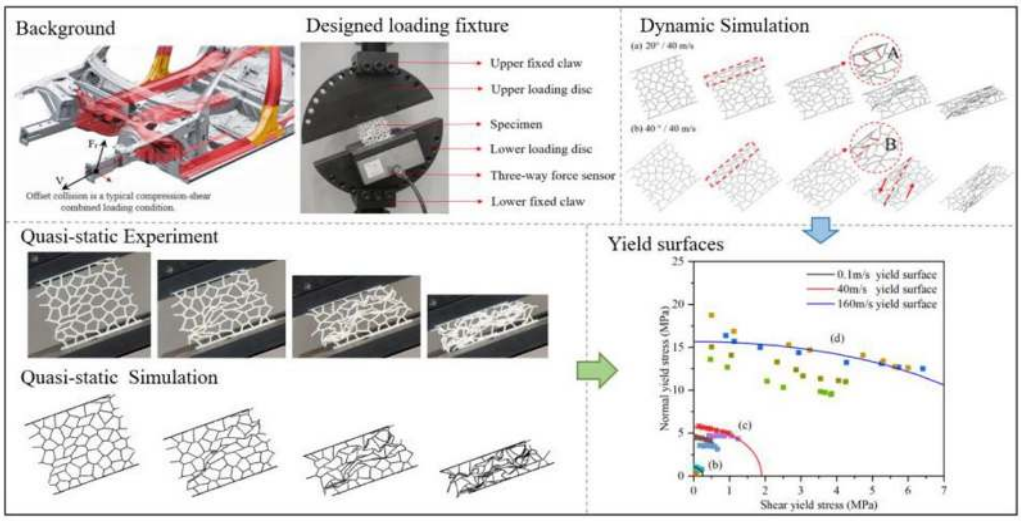

Received May 20, 2026. In revised form July 21, 2026. Accepted August 16, 2026. Available online August 19, 2026.
https://doi.org/10.1590/1679-7825/e9148

Latin American Journal of Solids and Structures. ISSN 1679-7825. Copyright © 2026. This is an Open Access article distributed under the terms of the Creative Commons Attribution License, which permits unrestricted use, distribution, and reproduction in any medium, provided the original work is properly cited.

1 INTRODUCTION

Random porous materials are widely found in nature. Through long-term natural selection, plants and animals have developed many high-performance random porous structures (San Ha N et al., 2020), such as luffa (Yin S et al., 2019), pomelo (Zhang W et al., 2019), and turtles (Rhee H et al., 2015). Various types of porous materials, particularly random honeycomb materials, are inspired by biological tissues with complex hierarchical structures. In recent years, these materials have attracted widespread attention due to their more stable mechanical responses and better energy absorption properties compared to traditional energy-absorbing materials (Qi C et al., 2021; Liang H et al., 2023; Wang S et al., 2021; Du F et al., 2023). Random porous materials are considered ideal materials for thin-walled structures and have broad application prospects in aerospace, military, and other engineering fields.

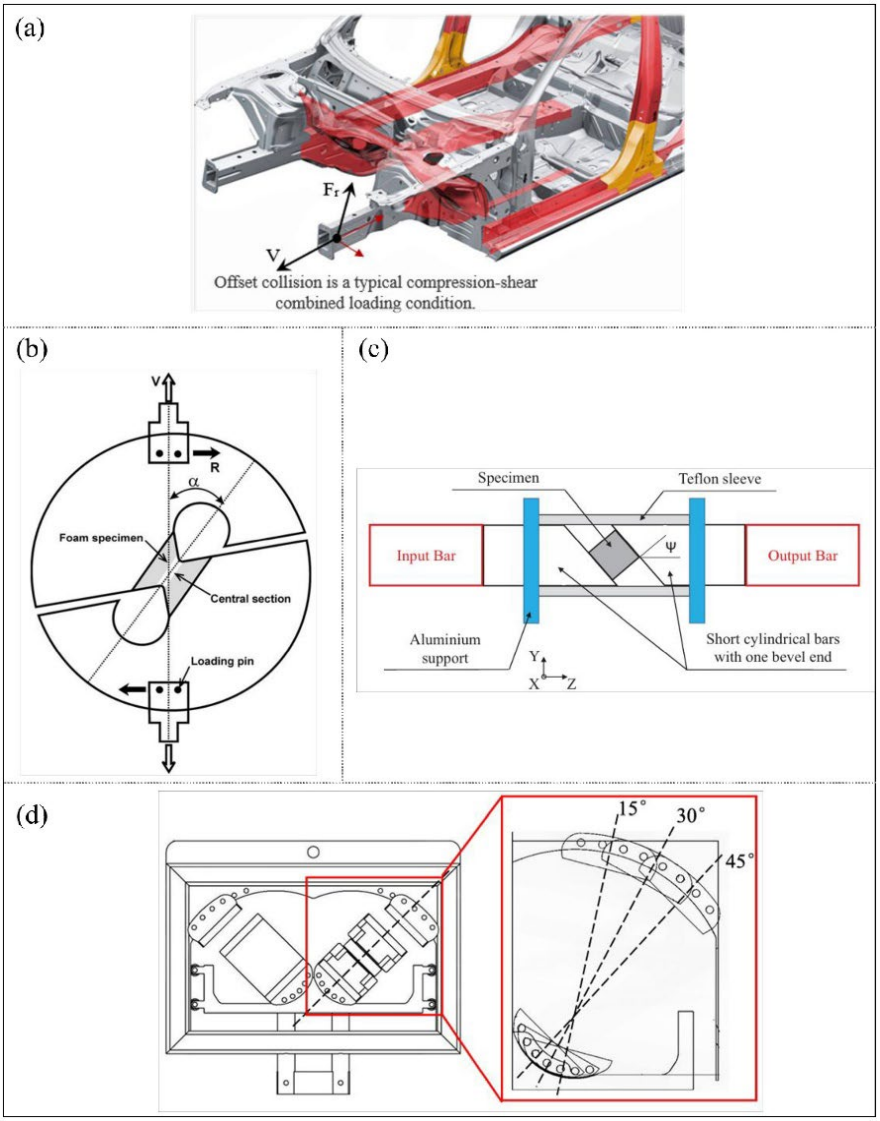

Figure 1. (a) Free body diagram of left crash box under offset loading; Compression-shear combined loading devices: (b) Foam sample loading test device (Doyoyo M et al., 2003) (c) A combined shear-compression device (Tounsi R et al., 2016) (d) Tri-axial load cell (Zhang D et al., 2019)

Random honeycomb materials are an essential subset of porous materials and are widely used as filler materials in various protective structures, such as automotive bumpers and the leading edges of aircraft wings. Under practical working conditions, materials are rarely subjected only to uniaxial compression or pure shear. Instead, they more often are subjected to complex loading conditions, especially the compression-shear combined loadings. For example, the offset collision is a typical compression-shear combined condition (Fig. 1(a)). To explore the feasibility of porous materials as lightweight and efficient energy-absorbing materials under complex loading conditions, their mechanical responses under compression-shear

combined loading have attracted increasing research attention. Early studies experimentally investigated the yield characteristics of porous materials. Arcan et al. (1978) proposed a testing device to simulate compression-shear loading conditions. Doyoyo et al. (2003) later improved this device (Fig. 1(b)) to study the yield behavior of butterfly-shaped foam specimens. However, this device could not achieve variable-angle compression-shear loading. In recent years, researchers have developed various compression-shear loading devices capable of variable-angle loading. For example, Zhao et al. (2022) used a variable-angle loading device to study the mechanical response of regular curved honeycombs under compression-shear combined loading. They found that the initial yield stress decreased by 16.2% as the curvature increased. Duan et al. (2020) achieved variable-angle dynamic compression-shear loading using a rotating Hopkinson bar and found that the deformation mode of honeycomb materials changed as the loading angle increased. In addition, the influence of porous-material meso-structures under compression-shear loading conditions has been investigated in detail. Tounsi et al. (2016) experimentally studied the dynamic response of aluminum-alloy honeycombs under compression-shear combined loading and found that the influence of the in-plane orientation angle β became more significant as the loading angle increased. The orientation angle βand the loading angle jointly affected the deformation mode. Zhang et al. (2019) experimentally investigated the mechanical responses of regular hexagonal honeycombs with different cell sizes under two loading velocities and three loading angles (15°, 30°, and 45°). They identified two deformation modes: non-inclined and inclined cell-wall deformation. The results showed that meso-structures significantly influenced the yield characteristics of porous materials, with different sensitivities at different loading angles. Although the aforementioned studies primarily investigated the mechanical properties of porous materials, comprehensive research on the influence of meso-structural characteristics under complex stress states remains limited.

Table 1. Proposed yield criteria of porous materials

	Yield criteria	Parameters
Eq. (1)	$\left(\frac{\sigma}{\sigma_{cr}}\right)^2 + (Acos^2\beta + Bsin^2\beta)\left(\frac{\tau}{\sigma_{cr}}\right)^2 = 1$	σ_{cr}: normal strength; A&B: material constants;
Eq. (2)	$f_0(\sigma_j\tau) = \left(\frac{\sigma}{\sigma_0}\right)^2 + \left(\frac{\tau}{\tau_0}\right)^2 - 1 = 0$	σ_0: normal yield strength; τ_0: shear yield stress;
Eq. (3)	$\left(\frac{\sigma}{\sigma_0 + c_1\frac{\rho v_i^2}{\varepsilon_d}}\right)^2 + \left(\frac{T}{T_0 + c_2\frac{\rho v_i^2}{\varepsilon_d}}\right)^2 = 1$	ρ: density of honeycomb; v_i: loading velocity; c_1 & c_2: fitting coefficients; ε_d: densification strain;

With the development of 3D printing (Abdulhameed O et al., 2019) and modeling technologies, we can now easily control the meso-structural parameters of random porous materials and fabricate plastic or metallic specimens (Askari M et al., 2020; Koju N et al., 2022). With the advancement of fixture design, specimen preparation techniques, and the integration of simulation technology (Lv Y et al., 2021), it has become possible to study the dynamic yield criteria of random honeycomb materials. Researchers have conducted a series of studies on the yield criteria of porous materials. Unlike continuous-media materials, porous materials exhibit higher plasticity and compressibility, making it more challenging to establish mathematical models of their meso-structural deformation mechanisms. As a result, researchers have developed various macroscopic yield criteria to predict their yield behavior under complex stress states (Hong S et al., 2006a; Hong S et al., 2006b; Mohr D et al. 2004; Hou B et al., 2011a; Hou B et al., 2011b). The commonly used yield criteria are listed in Table 1. In early studies, porous materials were idealized as rigid-plastic materials. When used as energy absorption devices, the normal and shear plateau stresses of porous materials were used to determine the yield surface. For example, Hong et al. (2006a; 2006b) proposed a phenomenological yield function for honeycombs with different in-plane orientation angles based on the normal compressive strength and shear strength of honeycomb materials under compression-shear combined loading. They suggested that a quadratic curve is suitable for honeycombs under quasi-static and dynamic combined loading, as expressed in Eq. (1). In their experimental study of regular aluminum honeycombs under multiaxial loading, Mohr and Doyoyo (2004) neglected the irreversible deformation of the honeycomb meso-structure before collapse and determined the initial yield surface based on the onset of plastic collapse. They found that the yield surface took an elliptical form in stress space, as shown in Eq. (2). This equation has been widely used to study the initial yield characteristics of various honeycomb materials. For instance, based on the uniaxial compressive and shear yield stresses of honeycombs derived by Ashby et al. (2013, 2016), Zhang et al. (2019) used Eq. (2) to determine the macroscopic yield surfaces of three types of regular honeycombs with different cell sizes.

Luo et al. (2023), in their study of the static and dynamic yield characteristics of star-shaped expanding honeycombs, used Eq. (2) to predict the initial yield behavior of expanding honeycomb materials and introduced the inertial effect induced by the loading velocity, as shown in Eq. (3).

In summary, existing studies have established an important foundation for understanding the deformation mechanisms and macroscopic yield behavior of honeycomb materials under compression-shear combined loading. However, most previous studies have focused on regular hexagonal, curved, or other deterministic configurations. In random honeycombs, the cell shapes, orientations, and weak regions exhibit significant spatial variability, and their local collapse mechanisms and mechanical responses under compression-shear combined loading have not yet been systematically clarified. In addition, existing studies have generally concentrated on the influence of individual structural parameters on the resulting mechanical properties, while the coupled effects of meso-structural parameters, loading angle, and loading velocity have received less attention. Therefore, it is necessary to develop an experimental method capable of applying controlled compression-shear combined loading and to combine experiments with dynamic simulations to systematically reveal the crushing mechanisms governing the compression-shear yield behavior of random honeycomb materials.

To address these issues, random honeycomb specimens with different irregularities, cell-wall thicknesses, and cell sizes were designed based on Voronoi tessellations and fabricated using additive manufacturing. A variable-angle compression-shear combined loading fixture based on a concentric-circle positioning principle was also independently designed. A tri-axial force sensor was used to synchronously measure the force components in different directions, which were then converted into the corresponding stresses. On this basis, quasi-static experiments were first conducted to systematically investigate the effects of loading angle and meso-structural parameters on the mechanical responses, deformation-band evolution, and cell-wall collapse mechanisms of random honeycombs. Subsequently, a finite element model accounting for the strain-rate sensitivity of base material was established to reveal the dynamic deformation mechanism by which random honeycombs transition from a random collapse mode to transitional and impact modes with increasing loading velocity. The relative contributions of loading angle and loading velocity to the normal and shear yield stresses were also quantitatively analyzed. Finally, a phenomenological yield criterion incorporating both meso-structural characteristics and loading velocity was established. The main contribution of this study is the integration of controlled compression-shear experiments, random meso-structural parameter analysis, and yield-surface prediction within a unified research framework, providing a theoretical basis for the design of random honeycomb materials used in offset collisions and energy-absorbing structures subjected to combined impacts.

2 MODELING AND VALIDATION

2.1 Configuration design

The random honeycomb material model is established based on 2D Voronoi diagrams. The generation process is presented in Figs. 2(a-c) (Luo G et al., 2024). Voronoi diagrams are generated using Python, and their edges and points are translated and trimmed. An Abaqus modeling program is developed to reconstruct the geometric information in the sketch module. Random honeycomb shell models are then created using the extrusion command, as shown in Fig. 2(d).

In this paper, the model dimensions are 70 mm in width along the x-axis, 70 mm in length along the y-axis, and 20 mm in thickness along the z-axis. Random honeycomb models with different meso-structural parameters, including irregularity, cell-wall thickness, and cell size, are established. The model labeled R02N60T12 represents a random honeycomb model with an irregularity of 0.2, 60 nucleation points, and a cell-wall thickness of 1.2 mm. The other models follow the same naming convention, as shown in Table 2.

The irregularity of the 2D Voronoi diagram nucleation point distribution is represented by R (Li K et al., 2007).

$$R = 1 - \frac{\delta}{\delta_0} \tag{4}$$

$$\delta_0 = \sqrt{2S_0/\sqrt{3}N} \tag{5}$$

where δ is the minimum distance between two nucleation points, δ_0 represents the minimum distance between hexagon nucleation points when filling a given area S_0 with N regular hexagons.

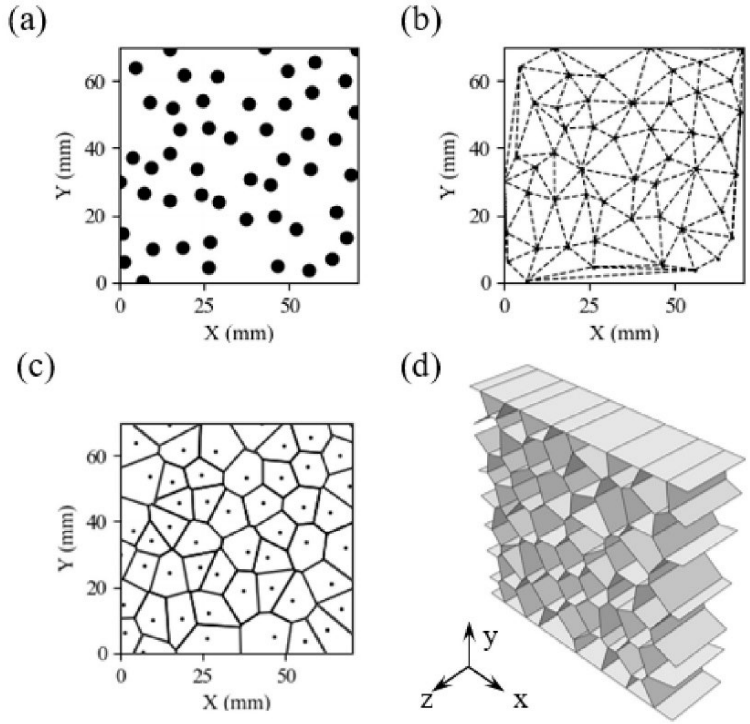

Figure 2. The process of generating a Voronoi diagram (Luo G et al., 2024): (a) Generation of random points (b) Construction of the Delaunay triangulation (c) Creation of the Voronoi diagram; (d) Shell element random honeycomb material models.

Additionally, the relative density of the random honeycomb material is denoted by $\bar{\boldsymbol{\rho}}$, as shown in Eq. (6).

$$\bar{\rho} = \frac{\rho_v}{\rho_s} = \frac{T}{LW}\sum l_i \tag{6}$$

where ρ_v is the density of the random honeycomb model, ρ_s is the density of the base material, T is the cell wall thickness, L and W represent the model length in the x-axis and y-axis, and l_i is the cell wall length.

A previous study (Luo G et al., 2023) found that, when the primary meso-structural parameters are kept constant, different models generated with the same irregularity exhibit very similar mechanical properties and can therefore be considered equivalent.

Table 2. Random honeycomb material models and their relative densities

Model name	R02N60T08	R02N60T12	R04N60T12	R06N60T12	R08N60T12	R02N80T12	R02N125T08
Relative density	0.165	0.248	0.247	0.248	0.253	0.271	0.242

2.2 Finite element model

Finite element simulations of the in-plane compression-shear combined loading of random honeycomb materials were conducted using Abaqus/Explicit, and the specimens were fabricated by 3D printing. A Raise3D E2 Pro 3D printer was used in this study. PolyMax™ polylactic acid (PLA) was selected as the printing material. The printing parameters were determined through a series of preliminary tests as follows: a layer height of 0.1 mm, a nozzle diameter of 0.4 mm, a global printing speed of 50 mm/s, an out-of-plane printing direction, an infill density of 100%, and a nozzle temperature of 205 °C. These parameters were used to fabricate all random honeycomb specimens and tensile specimens for characterizing the constitutive behavior of the base material. Quasi-static tensile tests, as shown in Figs. 3(a–b), indicated that the elastic modulus and Poisson's ratio of PLA were 1.905 GPa and 0.3, respectively. All printed specimens were visually inspected before testing. No obvious macroscopic defects, such as incomplete cell walls or interlayer separation, were observed. Based on the dynamic SHPB test results shown in Figs. 3(d–e), the Johnson–Cook model was used to describe the strain-rate-dependent stress enhancement of PLA (Luo G et al., 2023). The expression of the Johnson–Cook model is given in Eq. (7).

$$\frac{\sigma_y^d}{\sigma_y^0} = 1 + Cln\left(\frac{\dot{\varepsilon}}{\dot{\varepsilon}_0}\right) \tag{7}$$

where *σd y* is dynamic yield stress, *σ0 y* is quasi-static yield stress, $\dot{\varepsilon}$ and $\dot{\varepsilon}_0$ represent loading strain rate and reference strain rate, and *C* is material constant. The strain-rate sensitivity parameter *C*=0.07024 was calculated from the true stress-strain curves obtained at strain rates of 0.01 and 0.1 s^{-1}. Based on this parameter, the Johnson–Cook model predictions at 800 and 3000 s^{-1} showed good agreement with the SHPB test results. Therefore, the model was considered to be validated over the strain-rate range involved in the dynamic simulations conducted in this study.

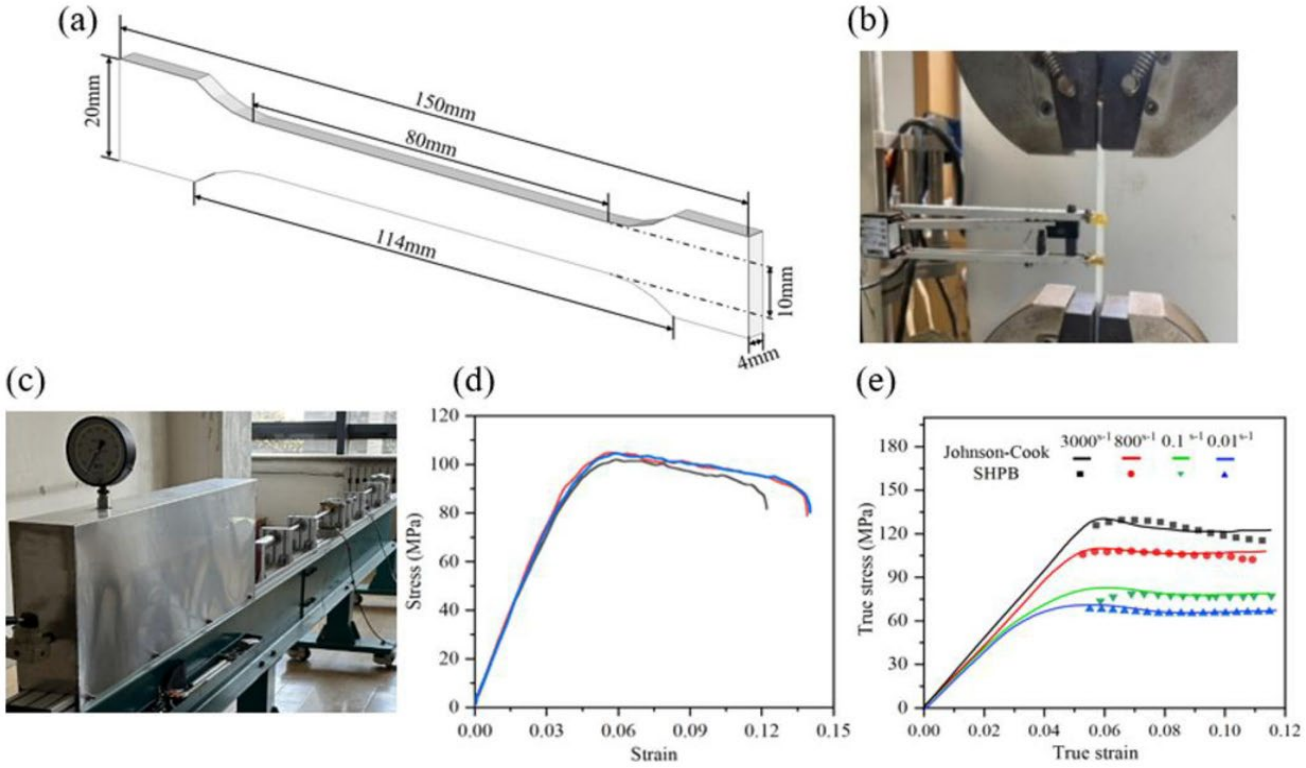

Figure 3. Quasi-static tensile test: (a) Specimen dimensions (b) Tensile test setup; Dynamic SHPB test: (c) SHPB test setup (d) Stress-strain curves of 800 s-1 test (e) Real stress-strain curves at different strain rates and Johnson Cook model curves (Luo G et al., 2023).

By varying the loading velocity *v* and the angle *α* between the specimen axis and the loading direction, different loading velocities and angles were applied to the finite element model. The loading plate and support plate were modeled using R3D4 discrete rigid elements, while the random honeycomb was modeled using S4R shell elements. Five integration points were defined through the cell-wall thickness to ensure model convergence. Based on mesh convergence tests using different mesh sizes, the mesh size was set to 1 mm. General contact with a friction coefficient of 0.2 was defined between the random honeycomb and the loading plate (Luo G et al., 2023; Wang S et al., 2020; ASTM, 1991; Feng G et al., 2021). To prevent out-of-plane buckling of the random honeycomb during loading, all degrees of freedom of the upper loading plate, except that in the loading direction, were constrained, and a constant loading velocity was applied. All degrees of freedom of the lower support plate were constrained, and the lower end of the random honeycomb was tied to the lower support plate. According to the quasi-static and dynamic drop-weight test results of the random honeycomb specimens, as shown in Figs. 4 and 5, no evident fracture was observed. Therefore, initial material defects and damage were not included in the finite element model. The finite element model established according to the experimental setup is shown in Fig. 4(b).

To fully validate the accuracy of the finite element model under compression-shear combined loading, quasi-static compression-shear combined loading tests were conducted. The variable-angle compression-shear combined loading fixture designed in this study is shown in Fig. 4(a). The compression-shear fixture was designed based on a concentric circular geometry. The angular positioning holes in the upper and lower loading discs share the same geometric center, through which the loading axis of the testing machine passes. Therefore, the resultant load acts nominally through the center of the fixture, minimizing systematic eccentricity and additional bending moments. After the loading angle was

selected, the loading discs were fastened to the clamps using bolts, and their relative orientation remained unchanged throughout the test. Both ends of the specimen were inserted into positioning grooves that were 70 mm long, equal to the specimen edge length. These grooves prevented gross end sliding and rigid-body rotation. The shear load was therefore transmitted primarily through geometric constraint and bearing contact between the specimen ends and the groove walls, rather than solely through uncontrolled friction at flat-platen interfaces. The loading angle α denotes the angle between the prescribed loading direction and the initial specimen axis. This nominal angle remained constant throughout the test. The normal and shear axes of the triaxial load cell were aligned with the local normal and shear directions of the specimen, respectively.

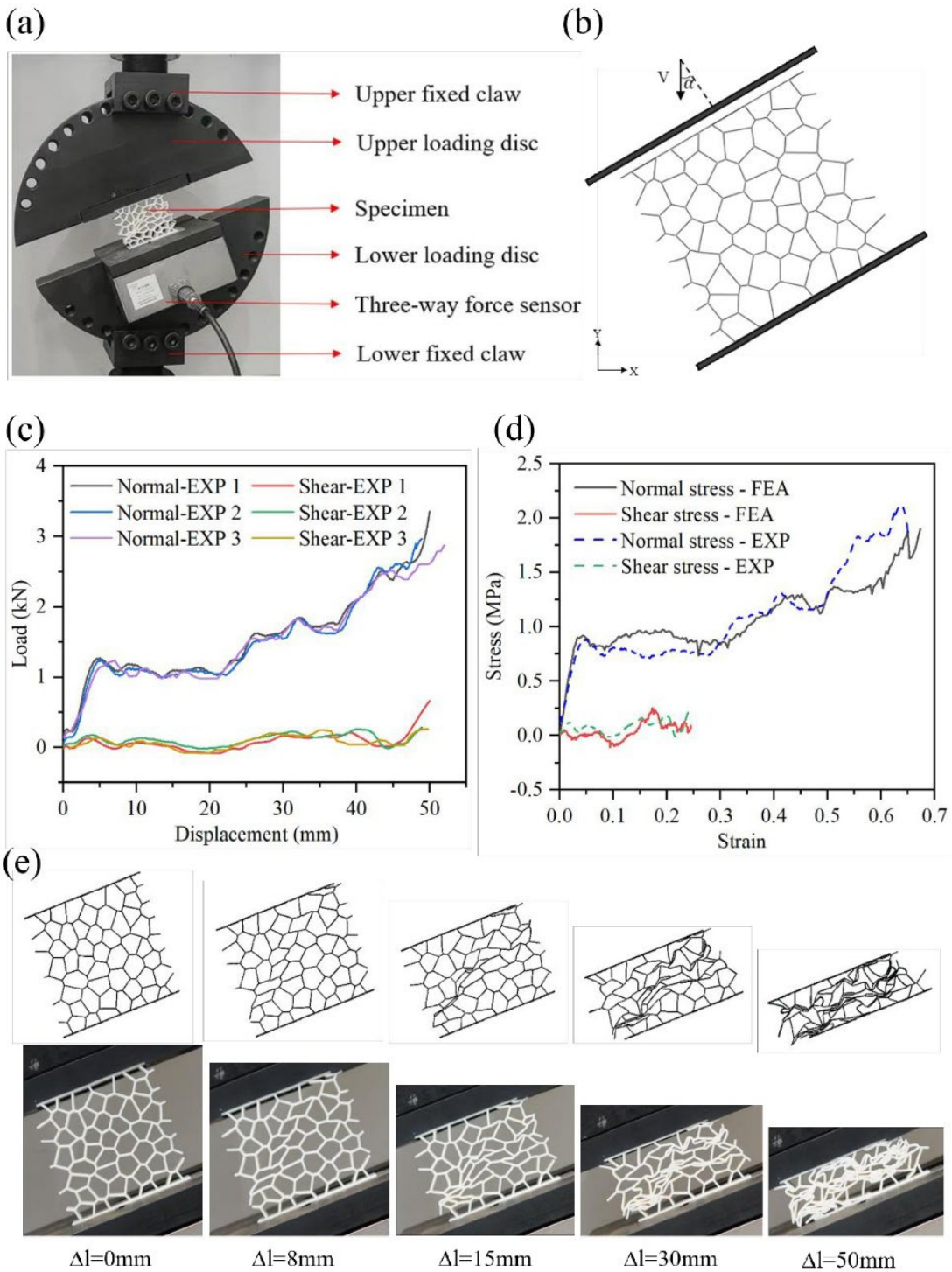

Figure 4. Compression-shear combined loading system: (a) Compression-shear combined loading fixture; (b) Finite element model under compression-shear combined loading; (c) Repeatability test results: specimen R02N60T12 at a loading angle of 20°; Experimental and numerical results for R02N60T12: (d) comparison of stress-strain curves; (e) comparison of deformation modes.

The quasi-static compression-shear combined loading tests were conducted using a SANS CMT-5205 universal testing machine, with the upper platen speed set to 4 mm/min. A Shanghai Naichuang FC3D160 triaxial force sensor was used to measure the normal and shear loads applied to the specimen, while a digital camera was used to record the deformation process. Three repeated tests were performed for each specimen. The quasi-static experimental results were then compared with the numerical simulation results. Fig. 5(c) presents the repeatability results for specimen R02N60T12 at a loading angle of 20°. The curves show good agreement in both load level and overall trend, indicating satisfactory experimental repeatability. Figs 5(d–e) present the comparison between the experimental and numerical results for specimen R02N60T12. The normal and shear stress-strain curves obtained from the experiments and simulations are in good agreement in terms of stress level and overall trend, and the predicted deformation mode also agrees well with the experimental observations.

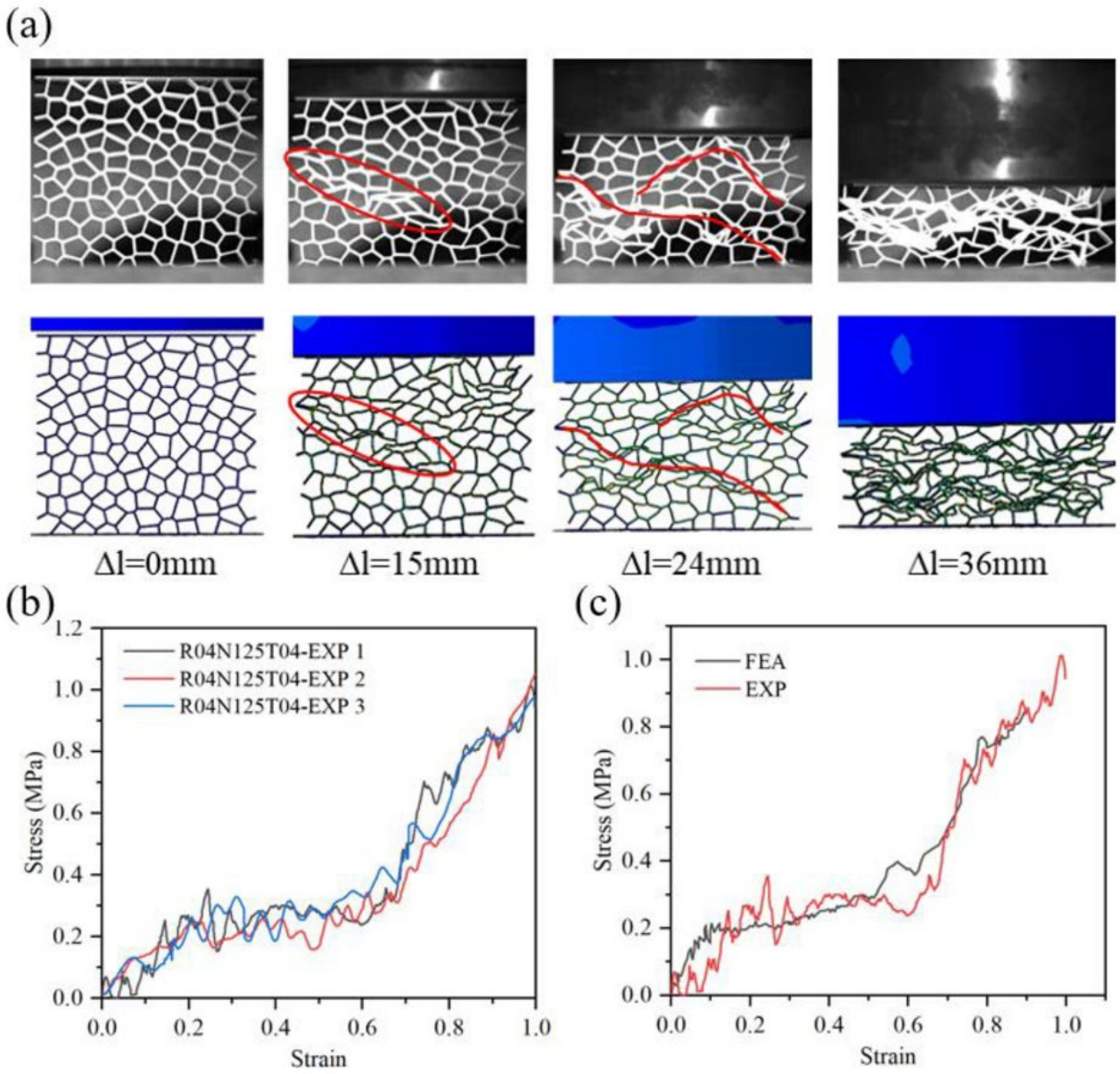

Figure 5. (a) Comparison of deformation modes between the experiment and simulation; Drop-weight test and numerical simulation results: (b) Repeatability test results (c) Comparison of stress-strain curves between the experiment and simulation (Luo G et al., 2023).

To further validate the accuracy of the dynamic finite element model of the random honeycomb material, dynamic compression tests were conducted (Luo G et al., 2023). The dynamic compression tests were performed using a WANCE DIT302Z-1 drop-weight testing machine. The impactor mass was 24.34 kg, and the impact velocity was set to 3.35 m/s.

A high-speed camera was used to record the deformation process, while the contact reaction force was measured using the force sensor of the drop-weight testing machine. To ensure the reliability of the results, three repeated tests were conducted on identical specimens. The comparisons between the experimental and numerical results, together with the repeated test results, are presented in Fig. 5. The simulated deformation modes and stress-strain curves show good agreement with the experimental results. Therefore, the established finite element model under compression-shear combined loading can be considered sufficiently accurate to reproduce the actual mechanical response of the random honeycomb specimens.

3 QUASI-STATIC MECHANICAL PROPERTIES

3.1 Effect of loading angle

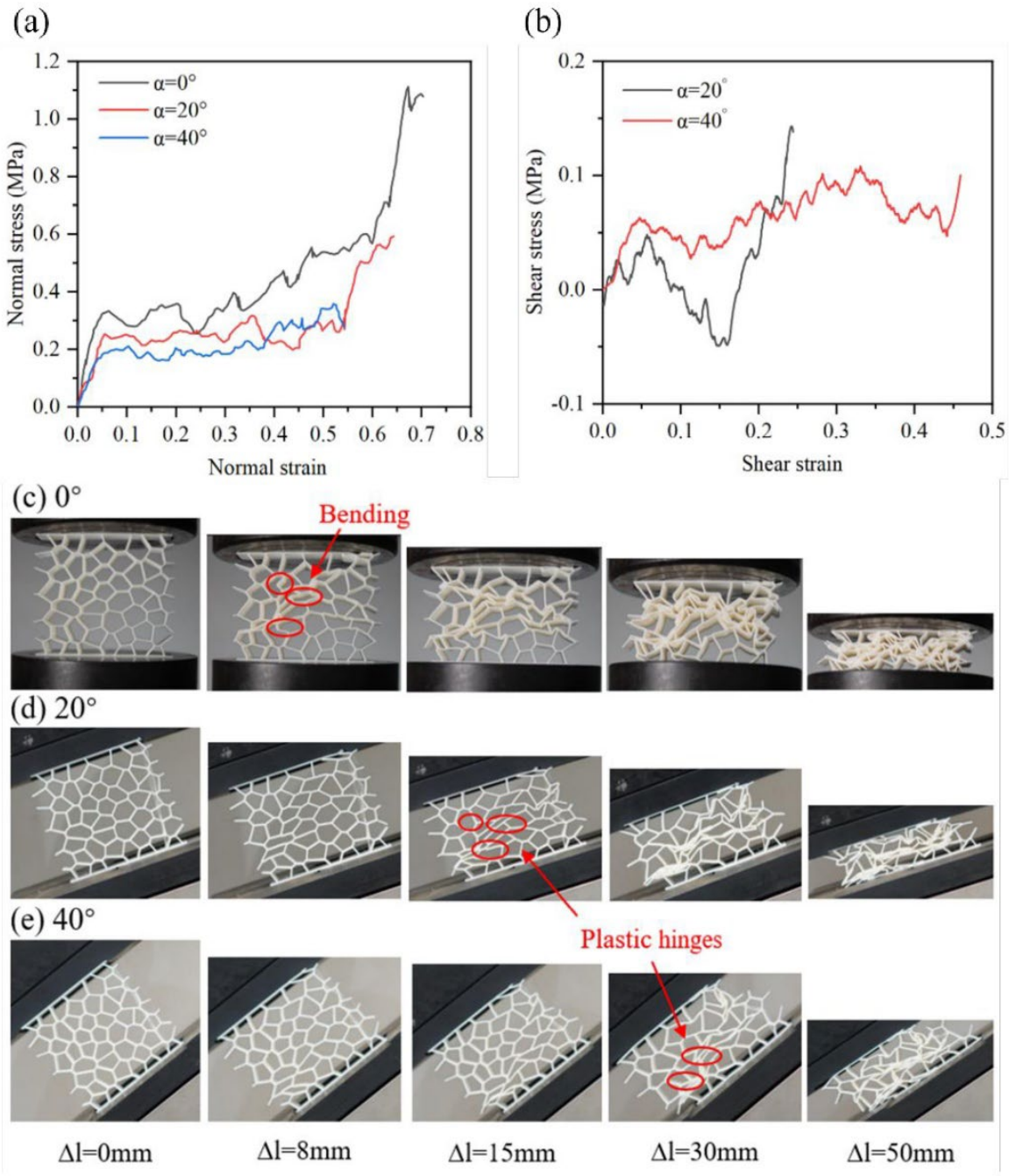

Figure 6. Stress-strain curves of the R02N60T08 specimen at different loading angles: (a) Normal stress (b) Shear stress; Deformation modes of the R02N60T08 specimen at different loading angles: (c) 0° loading angle (d) 20° loading angle (e) 40° loading angle.

For the R02N60T08 specimen, the stress-strain curves and deformation modes at loading angles of 0°, 20°, and 40° are compared in Fig. 6. The curves exhibit similar characteristics at different loading angles, with each curve comprising three stages: elastic, plateau, and densification. However, as the loading angle increases, the normal stress decreases, resulting in a lower normal yield stress and a higher shear yield stress. In addition, owing to the layer-by-layer collapse of the cells during deformation, the plateau stage of the stress-strain curves exhibits fluctuations. As the loading angle increases, the direction of cell collapse changes, leading to greater shear displacement, which extends the normal-stress plateau stage and increases the densification strain. Figs 6(c–e) show the deformation modes of the specimen at different loading angles. For the R02N60T08 specimen, changes in the loading angle affect the initial collapse location and the distribution of the deformation band. This is attributed to variations in cell-wall strength at different loading angles, which are related to the specific orientations of the cells. Under axial loading, the cell walls undergo bending deformation, whereas at loading angles of 20° and 40°, no significant cell-wall bending is observed. Instead, cell-wall deformation is primarily governed by plastic hinges.

3.2 Effect of irregularity

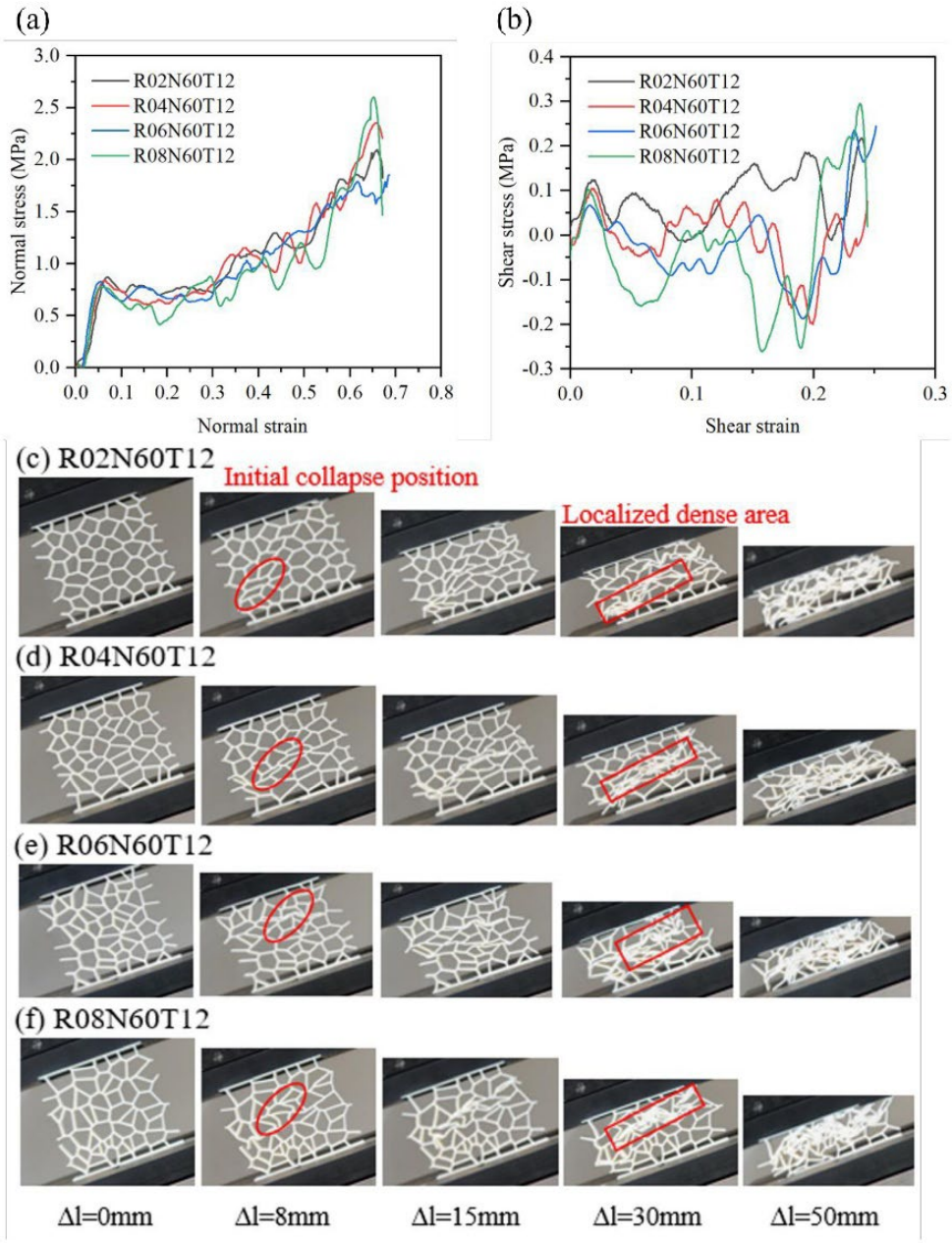

Figure 7. Stress-strain curves of specimens with different irregularities at 20° loading angle: (a) Normal stress (b) Shear stress; Deformation modes of specimens with different irregularities at 20° loading angle: (c) R02N60T12 (d) R04N60T12 (e) R06N60T12 (f) R08N60T12.

Based on the experimental results for specimens with different irregularities at a loading angle of 20°, the normal and shear stress-strain curves and deformation modes are shown in Fig. 7. As shown in Fig. 7(a), the normal stress levels of specimens with different irregularities are similar at a loading angle of 20°, with specimen R02N60T12 exhibiting slightly higher stress levels. In contrast, the shear stresses differ significantly among specimens with different irregularities. Although the shear yield stress levels are generally similar, specimen R02N60T12 exhibits a slightly higher shear yield stress. However, during subsequent loading, the direction of the shear stress differs among specimens with different irregularities. These differences are related to the deformation processes of the specimens. During loading, the cell walls are subjected to complex compression-shear combined loading. When the stress level reaches the normal or shear strength, the cells begin to collapse, as shown in Figs. 7(c–f). The cell-size distribution of the random honeycomb R02N60T12 is relatively uniform, making excessively long and weak cell walls less likely to occur than in honeycombs with higher irregularity. As a result, R02N60T12 exhibits higher normal and shear yield stresses. As loading progresses, the cells begin to collapse, and the cell walls rotate around plastic hinges. When the deformation reaches a certain level, the collapsed cell walls come into contact, leading to mutual compression and friction until the cells within the deformation band undergo local densification. During this process, both the normal and shear stresses fluctuate. In addition, differences in cell orientation among specimens with different irregularities lead to variations in the deformation-band distribution and the complex interactions between cells during deformation, resulting in differences in the direction of the shear stress.

3.3 Effect of wall thickness

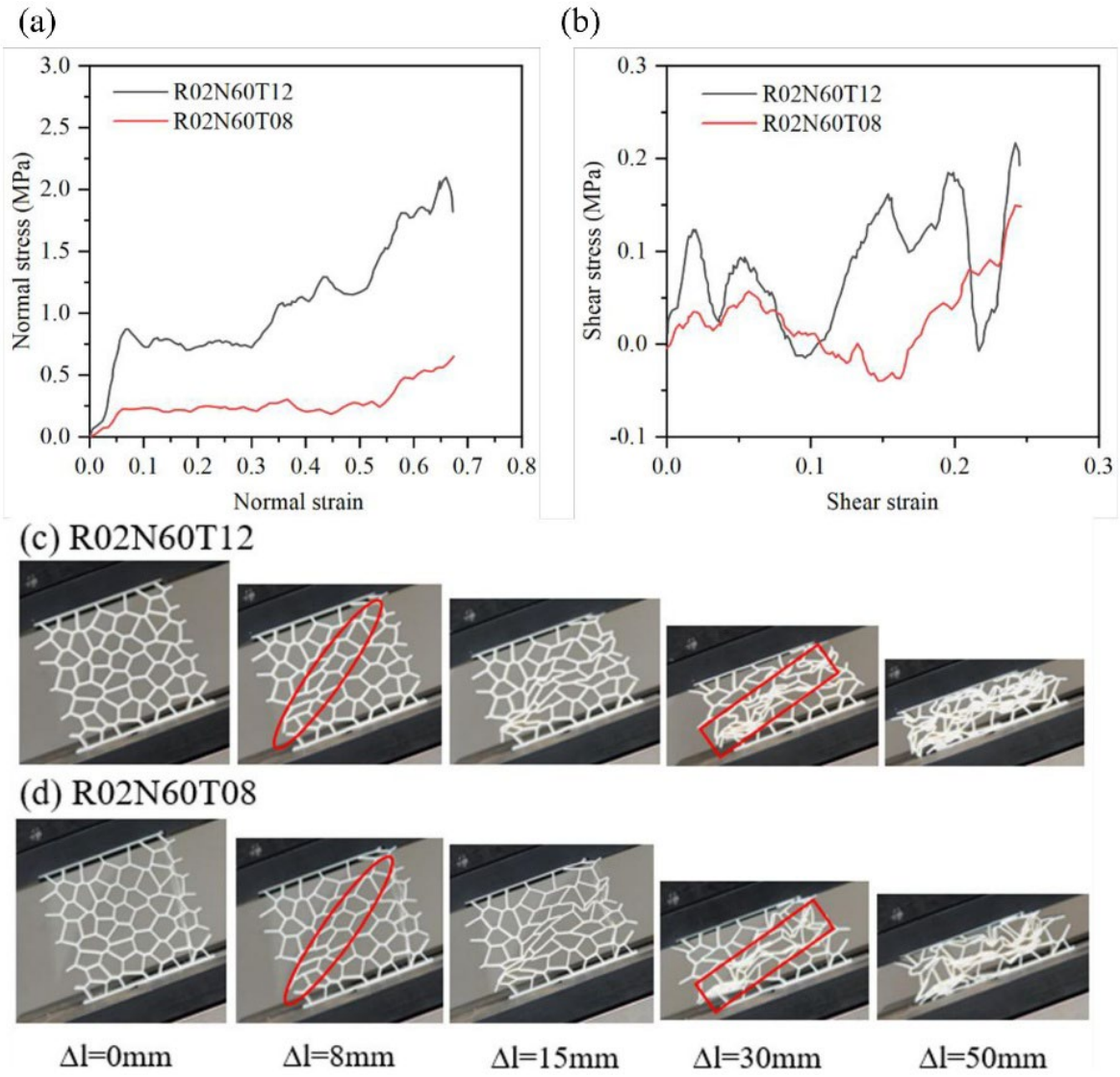

Figure 8. Stress-strain curves of specimens with different cell wall thicknesses at 20° loading angle: (a) Normal stress (b) Shear stress; Deformation modes of specimens with different cell wall thicknesses at 20° loading angle: (c) R02N60T12 (d) R02N60T08.

Based on the experimental results for specimens with different cell-wall thicknesses at a loading angle of 20°, the normal and shear stress-strain curves and deformation modes of specimens R02N60T12 and R02N60T08 are shown in Fig. 8. As shown in Figs. 8(a–b), both the normal and shear stresses increase with increasing cell-wall thickness. This is because thicker cell walls exhibit higher normal and shear strengths at different loading angles than thinner cell walls. Therefore, larger normal and shear loads are required to initiate cell-wall collapse, resulting in higher normal and shear stresses. In addition, during the deformation process from collapse to local densification, thicker cell walls require higher loads to yield, whereas local collapse instability causes a rapid decrease in load. Therefore, specimens with thicker cell walls exhibit greater fluctuations in normal and shear stresses than those with thinner cell walls. Furthermore, as shown in Figs. 8(c–d), specimens with different cell-wall thicknesses exhibit similar deformation modes during loading. Local collapse around plastic hinges occurs at the positions of weak cells, and the deformation-band distributions are very similar. Unlike under axial loading at a loading angle of 0°, changes in cell-wall thickness do not affect the meso-structural deformation mode of the cell walls under compression-shear combined loading at loading angles of 20° and 40°. No significant cell-wall bending is observed in specimen R02N60T08 during deformation.

3.4 Effect of cell size

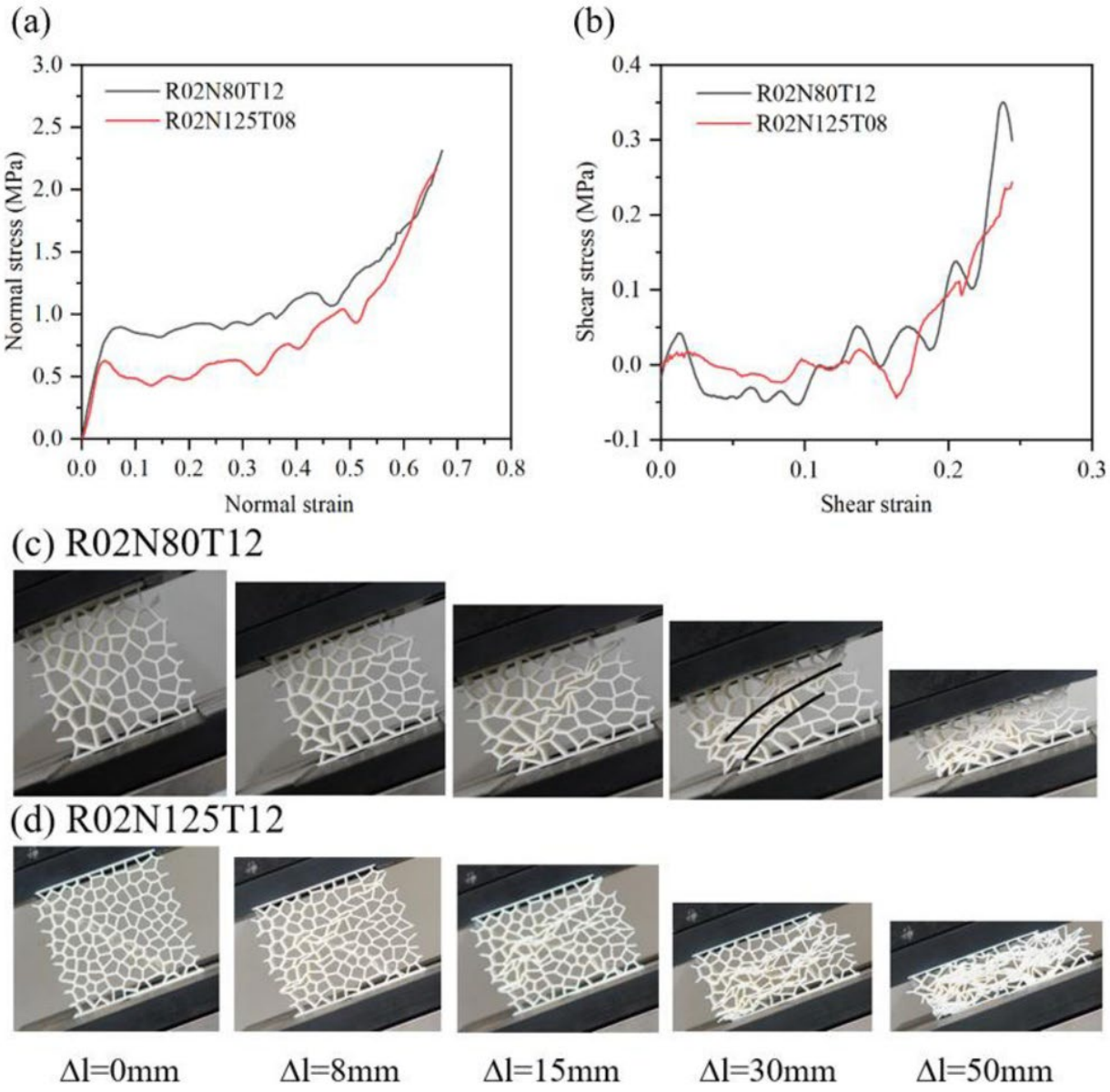

Figure 9. Stress-strain curves of specimens with different cell sizes at 20° loading angle: (a) Normal stress (b) Shear stress; Deformation modes of specimens with different cell sizes at 20° loading angle: (c) R02N80T12 (d) R02N125T08.

To analyze the effect of cell size on the mechanical response of random honeycomb specimens under compression-shear combined loading, the stress-strain curves and deformation modes of specimens with different cell sizes and cell-wall thicknesses but comparable relative densities at a loading angle of 20° are presented in Fig. 9. As shown in Figs. 9(a–b), at comparable relative densities, the normal and shear stress levels of specimen R02N125T08 are lower than those of specimen R02N80T12 at a loading angle of 20°. This contrasts with the similar stress levels observed for these specimens under axial loading. This result indicates that the meso-structures of random honeycomb materials and the loading angle significantly affect their mechanical responses. Compared with axial loading, under compression-shear combined loading, the specimen is subjected to normal and shear loads simultaneously, which affects the collapse and deformation modes of the cell walls. Specimen R02N125T08, with a smaller cell size, exhibits lower normal or shear strength at the collapse locations, resulting in changes in the positions of the deformation bands. In contrast, specimen R02N80T12, with fewer cells, exhibits only minor changes in the positions of the deformation bands. Therefore, under compression-shear combined loading, the stress levels of specimen R02N125T08 are significantly lower than those of specimen R02N80T12.

4 DYNAMIC MECHANICAL PROPERTIES

4.1 Dynamic deformation modes

Figs. 10(a–b) show the deformation process of the R04N60T12 model at a loading velocity of 40 m/s and loading angles of 20° and 40°. At a loading velocity of 40 m/s, the model enters the transitional mode, in which the strength of the cells within the wavefront region is lower than the amplitude of the plastic compression wave induced by loading. The cells near the loading end deform first, as observed at Δ*l*=8 mm. During the subsequent deformation process, more cells gradually yield. Unlike under quasi-static compression-shear combined loading, where the meso-structural deformation is primarily governed by rotation about plastic hinges, dynamic loading induces either cell-wall bending or rotation about plastic hinges. Localized deformation bands subsequently form until the random honeycomb model is fully crushed.

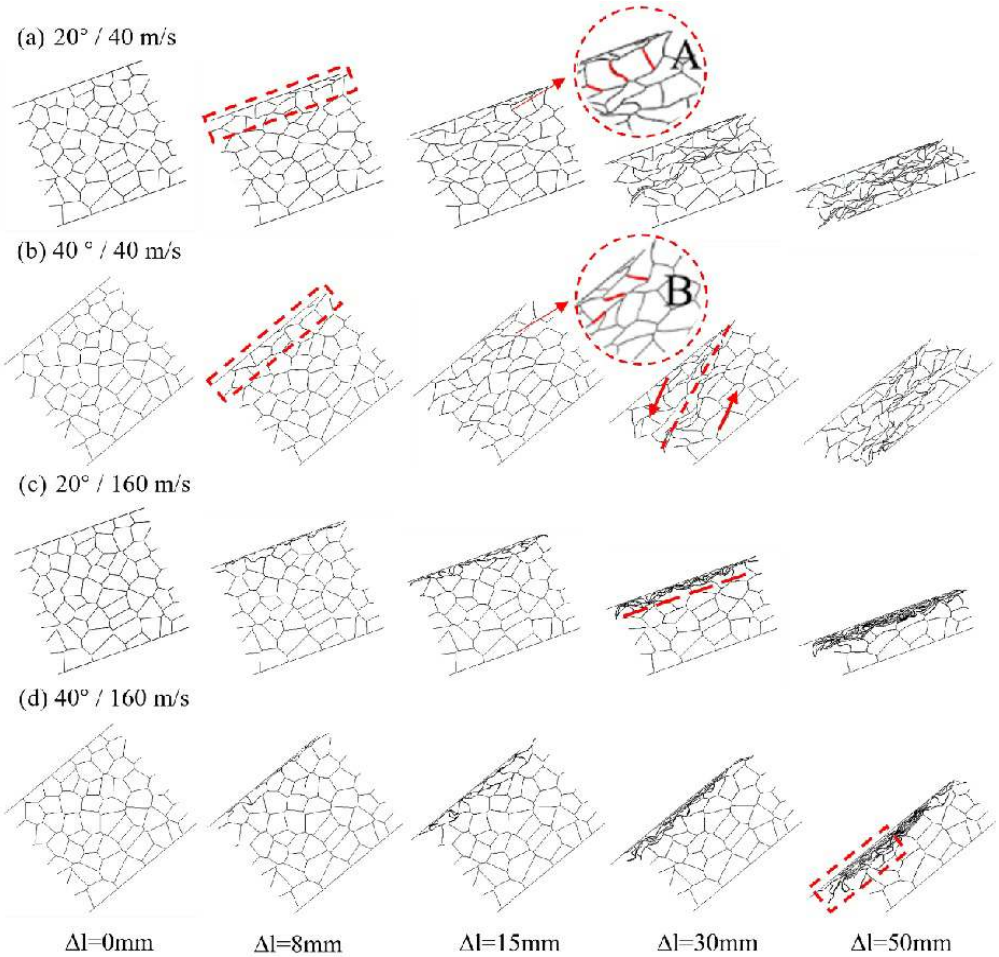

Figure 10. Deformation process of the R04N60T12 model under 40 m/s: (a) 20° loading angle (b) 40° loading angle; Deformation mode of the R04N60T12 model under 160 m/s: (c) 20° loading angle (d) 40° loading angle.

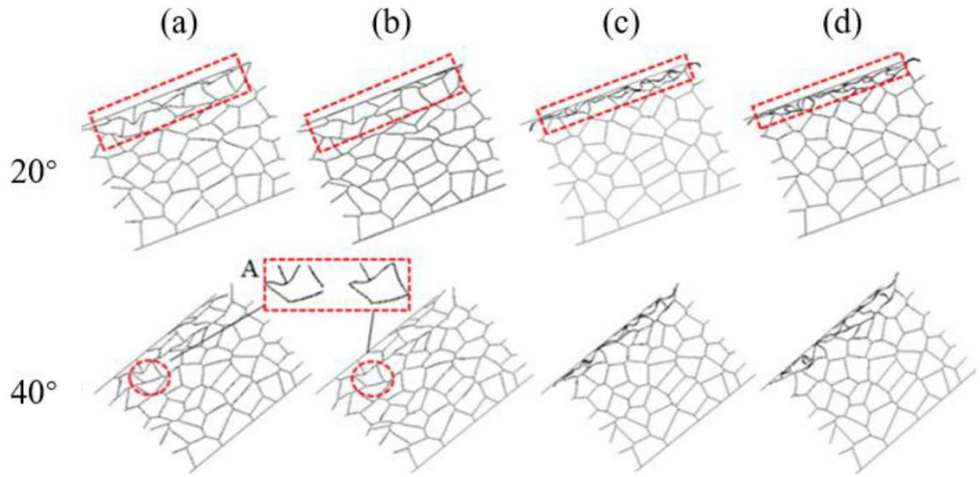

Figure 11. Deformation patterns of R04N60T12 at Δ*l*=15mm: (a) base material with strain rate insensitivity at 40 m/s velocity (b) base material with strain rate sensitivity at 40 m/s velocity (c) base material with strain rate insensitivity at 160 m/s velocity (d) base material with strain rate sensitivity at 160 m/s velocity.

In addition, an increase in the loading angle results in greater shear displacement, causing relative movement of the cells along the central deformation band, as shown in Fig. 11. In the transitional mode, this relative movement is accommodated through cell-wall bending and rotation about plastic hinges. Unlike under quasi-static compression-shear combined loading, an increase in the loading angle causes some cell walls to transition from bending deformation to plastic-hinge formation, as indicated by points A and B in Figs. 11(a–b), with point A representing intensified flexural deformation. In contrast, under quasi-static compression-shear combined loading, although the position of the deformation band changes with the loading angle, the meso-structural deformation mode of the random honeycomb material remains primarily governed by plastic hinges. Figs. 11(c–d) show the deformation process of the R04N60T12 model at a loading velocity of 160 m/s and loading angles of 20° and 40°. At a loading velocity of 160 m/s, the model enters the impact mode, in which the cells are sequentially crushed and compacted. As each layer of cells collapses, the cell walls initially undergo bending deformation under the action of the plastic shock wave. As the loading plate moves in the shear direction, the bending deformation gradually increases. Once the deformation reaches a certain level, the cell walls compress the next layer of cells, causing progressive compaction, while the shock wave continues to propagate toward the wavefront. In addition, the high stress induced by the shock wave causes cell-wall bending at different loading angles. As the loading angle increases, the shear tensile effect causes the deformation band to concentrate near the left end of the model but does not alter the meso-structural deformation mode of the cell walls.

4.2 Dynamic stress-strain curves

To analyze the dynamic mechanical response of random honeycomb materials under dynamic compression-shear combined loading, simulations were performed at different loading velocities and loading angles of 20° and 40° for models with different meso-structural parameters. The detailed analysis is presented below.

Fig. 12 shows the normal and shear stress-strain curves of models with different irregularities, cell-wall thicknesses, and cell sizes at a loading velocity of 40 m/s. At this velocity, the models are in the transitional mode and begin to undergo gradual crushing. The cells within the wavefront enter the plastic deformation stage, and the yield stress initially increases owing to the strain-rate sensitivity of the base material and inertial effects. Subsequently, the cells within the wavefront become unstable and collapse, leading to a rapid decrease in the normal and shear stresses. Owing to inertial effects, the stress levels during the plateau stage remain higher than those under static loading conditions. Finally, during the overall collapse process, the normal and shear stresses fluctuate and gradually increase.

Fig. 13 shows the stress-strain curves of models with different irregularities, cell-wall thicknesses, and cell sizes at a loading velocity of 160 m/s. At this velocity, all models enter a fully progressive crushing impact mode. Compared with the random and transitional modes, the cells near the loading end collapse layer by layer in the impact mode, resulting in significant fluctuations in both the normal and shear stresses. In addition, owing to the enhanced inertial effects and strain-rate effects of the base material, the yield stress and the stress levels in the plateau stage of each model increase further. Moreover, this layer-by-layer crushing mode allows the cells to deform more fully during loading, leading to an increase in the densification strain of the models, while no distinct densification stage is observed.

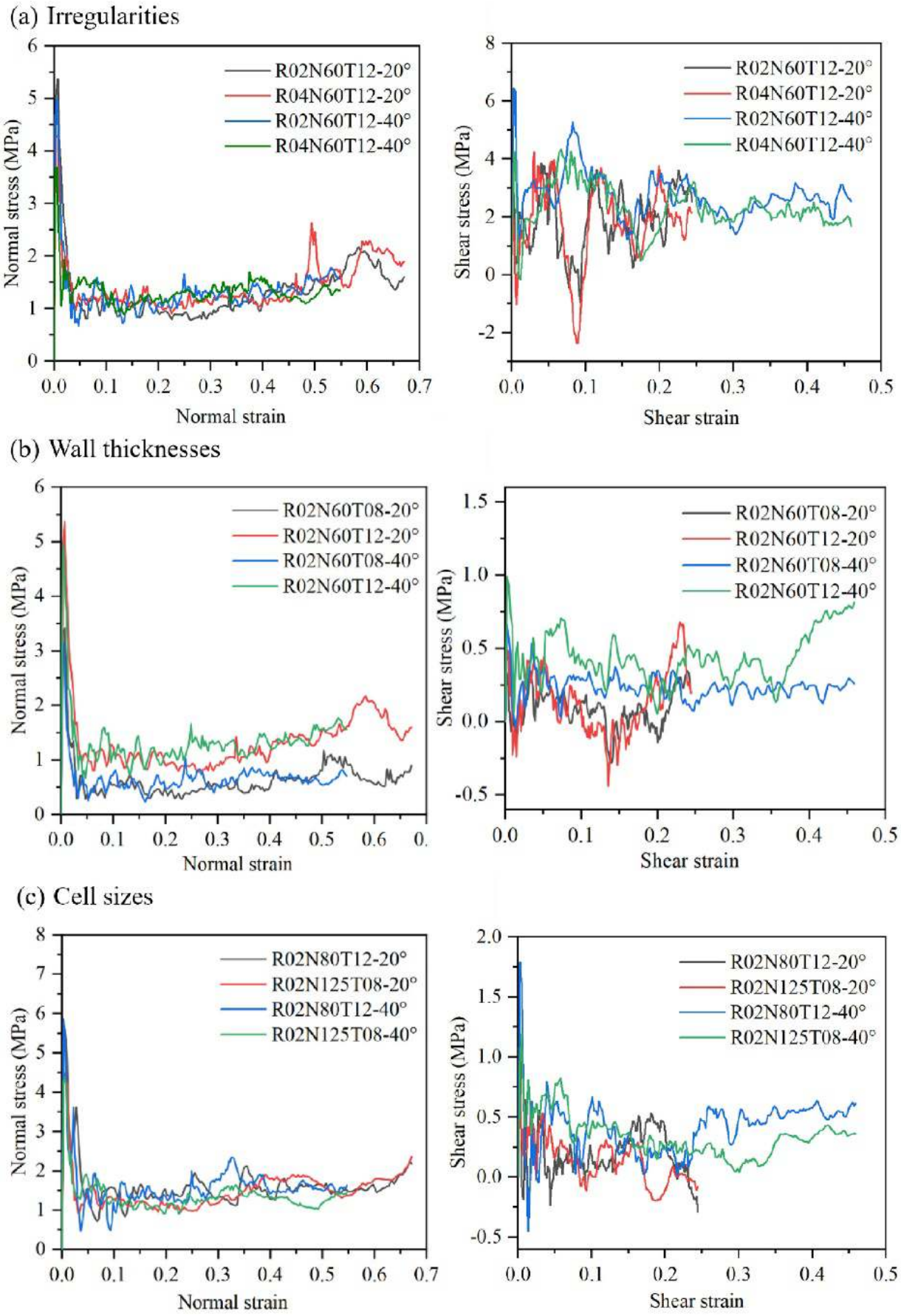

Figure 12. Stress-strain curves of models under 40 m/s at different loading angles with different (a) irregularities (b) wall thicknesses (c) cell sizes.

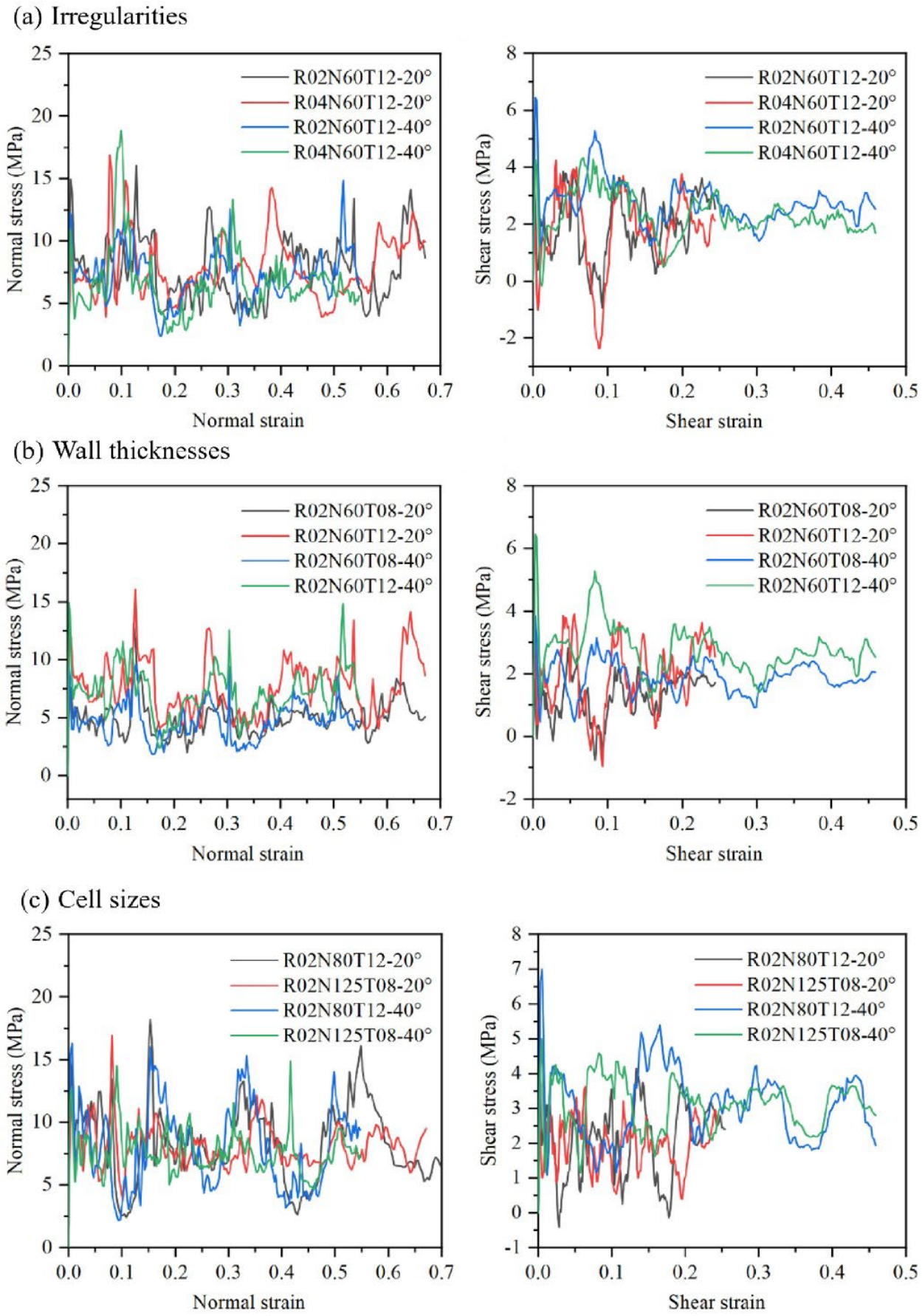

Figure 13. Stress-strain curves of models under 160 m/s at different loading angles with different (a) irregularities (b) wall thicknesses (c) cell sizes.

Combining the results of the static tests and dynamic simulations, it is found that, under the six static loading conditions, although the deformation modes change, the effects of the meso-structural parameters on the normal and shear stress-strain curves follow the same trends. These trends are related to the strength of the cells within the deformation band. Specifically, a lower irregularity results in slightly higher normal and shear stresses, an increase in cell-wall thickness leads to higher normal and shear stresses, and a reduction in cell size decreases both the normal and shear stress levels when the relative density is kept constant. In addition, the effect of the loading angle under static loading follows the same trend: as the loading angle increases, the normal stress decreases, whereas the shear stress increases.

Additionally, using the R04N60T12 model as an example, the effect of the strain-rate sensitivity of the base material on the stress-strain curves under compression-shear combined loading was investigated. Fig. 14 shows the normal and shear stress-strain curves of the R04N60T12 model at different loading velocities and loading angles of 20° and 40°. As shown in Fig. 14(a), at a loading velocity of 40 m/s, the strain-rate-sensitive base material exhibits a noticeable increase in normal yield stress at both loading angles of 20° and 40° compared with the strain-rate-insensitive base material. However, the shear stress curves are nearly identical in terms of overall trend and stress level, with only minor fluctuations at certain points. At a loading velocity of 160 m/s, the normal yield stress of the strain-rate-sensitive base material does not increase significantly compared with that of the strain-rate-insensitive base material. This is because inertial effects dominate at high loading velocities and weaken the relative contribution of strain-rate effects. In contrast to the results at 40 m/s, the shear stress of the strain-rate-sensitive base material increases significantly. At a loading angle of 40°, the increase in shear stress caused by strain-rate effects is greater than that at 20°, which is related to the deformation mode. At a loading velocity of 160 m/s, the model enters the impact mode, in which the cell walls collapse and are crushed in the shear direction. The strengthening effect associated with the strain-rate sensitivity of the base material therefore leads to a noticeable increase in shear stress. In contrast, at 40 m/s, the model is in the transitional mode, resulting in a less pronounced increase in shear stress.

5 YIELD STRESS AND YIELD SURFACE THEORY STUDY

5.1 Yield Stress

The compression-shear yield surface is an important tool for characterizing the mechanical properties of porous materials, particularly their yield behavior under compression-shear combined loading. To obtain this yield surface, simulations were performed for the R02N60T12 model at loading angles ranging from 0° to 40° and loading velocities of 0.1, 40, and 160 m/s. The resulting normal and shear yield stresses are presented in Figs. 15 and 16 and Tables 3 and 4.

Fig. 15 shows the variation in normal yield stress under different loading conditions. As the loading angle increases, the normal yield stress of the model decreases, whereas it increases with increasing loading velocity. Table 3 further presents the percentage increase in normal yield stress as the loading velocity increases from 0.1 to 40 m/s at different loading angles, as well as the percentage decrease in normal yield stress as the loading angle increases from 5° to 40° at different loading velocities. At a loading velocity of 0.1 m/s, the normal yield stress decreases from 1.03 to 0.71 MPa, corresponding to a reduction of 31%, as the loading angle increases from 5° to 40°. In contrast, at a loading angle of 5°, the normal yield stress increases from 1.03 to 5.76 MPa, corresponding to an increase of approximately 459%, as the loading velocity increases from 0.1 to 40 m/s. These results indicate that loading velocity has a considerably greater influence on the normal yield stress than loading angle.

The variation in shear yield stress under different loading conditions is shown in Fig. 16. As the loading angle increases, the shear yield stress of the model increases; it also increases with increasing loading velocity. Compared with the normal yield stress, the shear yield stress is less sensitive to changes in loading velocity and loading angle. Table 4 presents the percentage increase in shear yield stress as the loading velocity increases from 0.1 to 40 m/s at different loading angles, as well as the percentage increase in shear yield stress as the loading angle increases from 5° to 40° at different loading velocities. At a loading velocity of 0.1 m/s, the shear yield stress increases from 0.054 to 0.21 MPa as the loading angle increases from 5° to 40°, corresponding to an increase of approximately 289%. At a loading angle of 5°, the shear yield stress increases from 0.054 to 0.15 MPa as the loading velocity increases from 0.1 to 40 m/s, corresponding to an increase of approximately 178%. These results indicate that increases in both loading angle and loading velocity significantly enhance the shear yield stress. In addition, at a loading velocity of 40 m/s, the shear yield stress increases by 560% as the loading angle increases from 5° to 40°, which is substantially greater than the approximately 288% increase observed at a loading velocity of 0.1 m/s. Therefore, an increase in loading velocity enhances the influence of the loading angle on the shear yield stress.

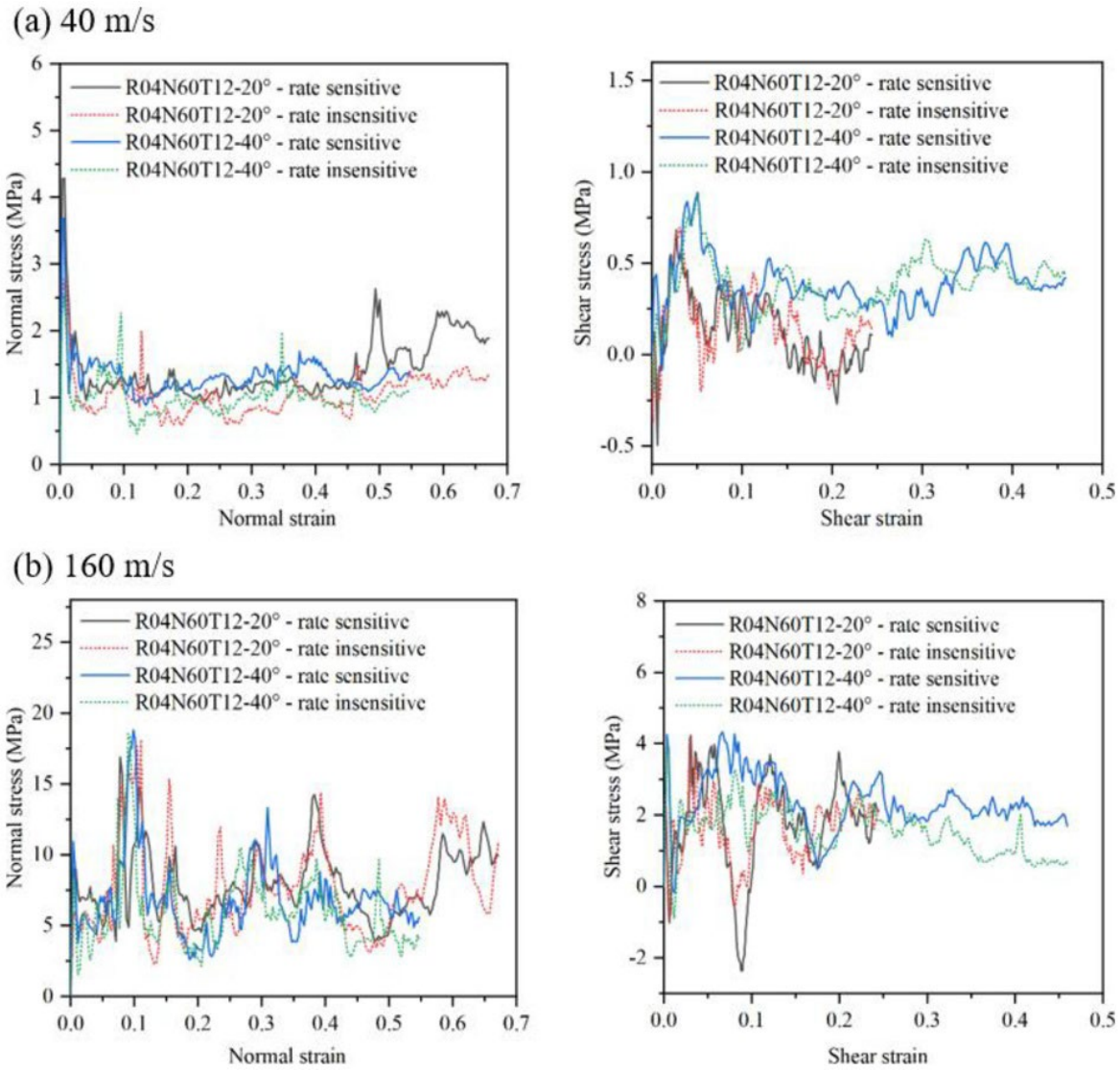

Figure 14. Stress-strain curves of R04N60T12 with different cell sizes at different loading angles under (a) 40 m/s (b) 160 m/s.

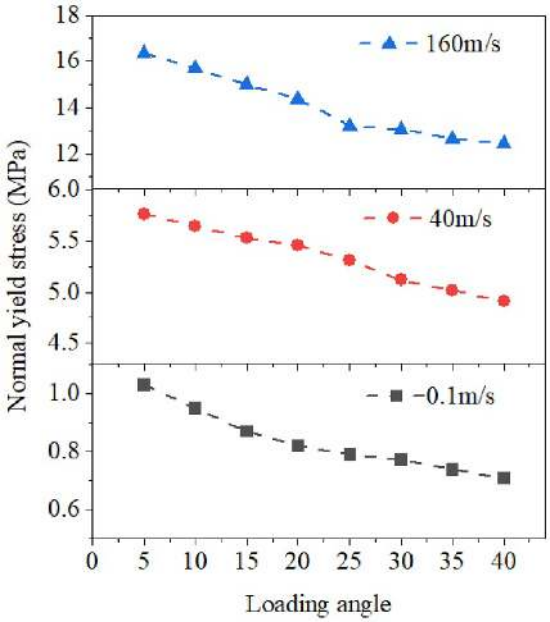

Figure 15. Trend of normal yield stress for R02N60T12

Table 3. Normal yield stress of R02N60T12 under different conditions

Conditions	5°	10°	15°	20°	25°	30°	35°	40°	Decrease
0.1m/s	1.03	0.95	0.87	0.82	0.79	0.77	0.74	0.71	31%
40m/s	5.76	5.65	5.53	5.46	5.31	5.12	5.02	4.91	14%
160m/s	16.33	15.69	15.00	14.37	13.21	13.07	12.65	12.47	23%
Increase	459%	494%	535%	565%	572%	564%	578%	591%	

Table 4. Shear yield stress of R02N60T12 under different conditions

Conditions	5°	10°	15°	20°	25°	30°	35°	40°	Increase
0.1m/s	0.054	0.08	0.10	0.13	0.15	0.17	0.18	0.21	288%
40m/s	0.15	0.26	0.39	0.48	0.63	0.82	0.95	0.99	560%
160m/s	0.90	1.14	1.87	2.94	4.28	5.26	5.73	6.42	613%
Increase	177%	225%	290%	269%	320%	382%	427%	371%	

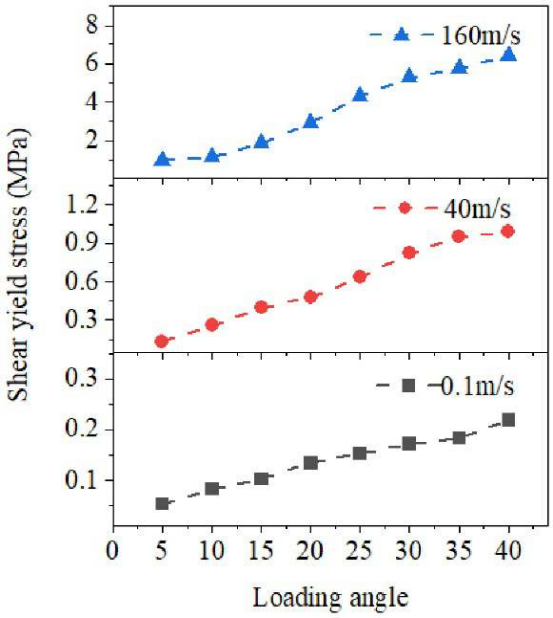

Figure 16. Trend of shear yield stress for R02N60T12

Based on the calculation and analysis of normal and shear yield stresses, it can be concluded that the normal yield stress of random honeycomb materials is primarily influenced by the loading velocity, with the effect of loading angle being relatively minor. In contrast, the shear yield stress is affected by both the loading angle and the loading velocity. In addition, under the loading conditions considered in this study, the shear yield stress of the random honeycomb materials is consistently lower than the normal yield stress.

5.2 Phenomenological Yield Criterion

In porous materials under combined compression-shear loading, researchers often establish yield criteria based on elliptical functions (Doyoyo M et al., 2003). Similarly, this paper establishes the yield criterion based on elliptical functions, as shown in Eq. (8).

$$\left(\frac{\sigma}{\sigma_d}\right)^2 + \left(\frac{\tau}{\tau_d}\right)^2 = 1 \tag{8}$$

where σ_d and τ_d represent the normal and shear yield stresses of the random honeycomb material.

Unlike continuous medium materials, porous materials exhibit higher plasticity and compressibility. Additionally, as discussed in the analyses of quasi-static and dynamic compression-shear combined loading, the mechanical response is

affected not only by the meso-structural parameters but also significantly by the strain-rate sensitivity of the base material under dynamic loading. Therefore, establishing a coupled mathematical model that reflects both the meso-structural deformation mechanisms and strain rate effects is challenging. Accordingly, a phenomenological yield criterion for the R02N60T12 model was established by incorporating only the loading velocity. The distributions of yield stress in the compression-shear stress space were then analyzed for models with other meso-structural parameters.

Based on the simulation results for loading velocities of 0.1 m/s, 40 m/s, and 160 m/s, the normal and shear yield stresses of the R02N60T12 model were calculated. A nonlinear implicit-function curve-fitting method was used to determine σ_d and τ_d at loading velocities of 0.1, 40, and 160 m/s, as shown in Table 5. The variation of yield stresses with loading velocity is shown in Fig. 17. Both the normal and shear yield stresses exhibit a linear relationship with the loading velocity. Respectively, a linear function with a positive intercept was used to determine the relationship between loading velocity and the normal and shear yield stresses. The fitting parameters A_1, B_1, A_2, and B_2 are provided in Table 6, and the established yield function is given by Eq. (9).

$$\left(\frac{\sigma}{A_1 v+B_1}\right)^2+\left(\frac{\tau}{A_2 v+B_2}\right)^2=1 \tag{9}$$

Table 5. Yield stresses of R02N60T12 at different loading velocities

	0.1m/s	**40m/s**	**160m/s**
σ_d(MPa)	1.03	5.70	15.68
τ_d(MPa)	0.25	1.98	9.52

Table 6. Fitting parameters

A_1	B_1	A_2	B_2
0.0897	1.489	0.0585	0.1223

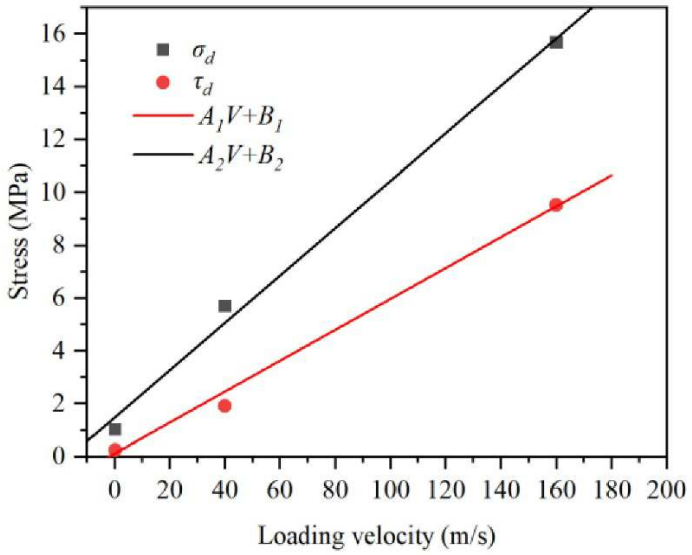

Figure 17. Yield stresses of R02N60T12 at different loading velocities

Using Eq. (9), the yield surfaces of the R02N60T12 model at different loading velocities can be calculated. The theoretical yield surfaces at loading velocities of 0.1, 40, and 160 m/s were compared with the numerical results. In addition, the yield stresses of other random honeycomb models with different meso-structural parameters are presented in Fig. 18. As shown in Fig. 18(a), both the normal and shear yield stresses increase with increasing loading velocity, causing the yield surface to expand outward. Figs. 18(b–d) show enlarged views at different loading velocities. A comparison of the yield-stress distributions of the R02N60T12, R04N60T12, and R02N60T08 models at different loading velocities indicates that a decrease in irregularity and an increase in cell-wall thickness enhance the normal and shear yield stresses of the random honeycomb material.

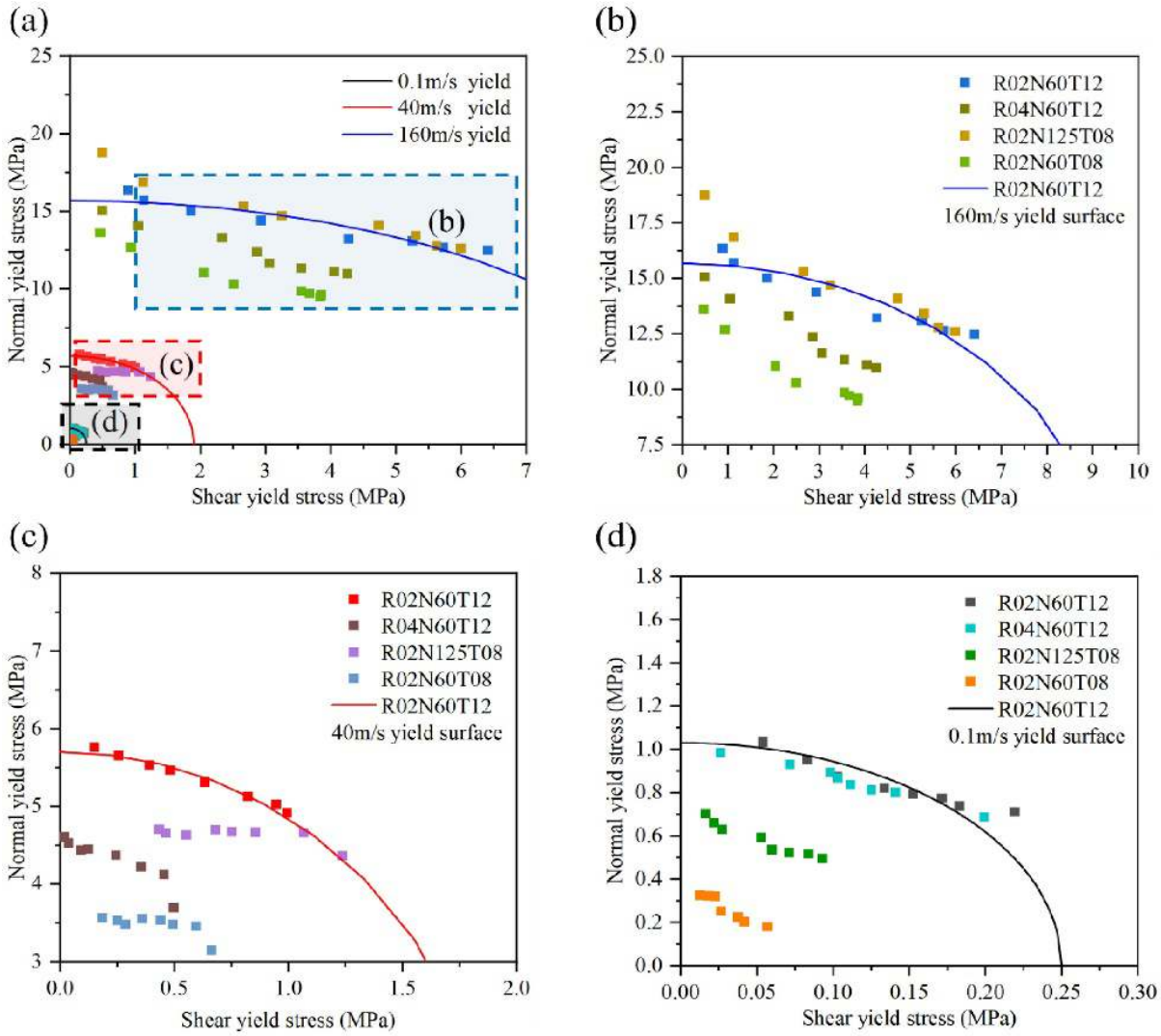

Figure 18. Yield stress of different models and yield surface of R02N60T12 at different loading velocities: (a) Schematic of yield surface (b) 160 m/s (c) 40 m/s (d) 0.1 m/s.

It can also be noted that although the relative density of R02N125T08 is higher than that of R02N60T12, the yield stress of R02N125T08 is lower than that of R02N60T12 at both 0.1 and 40 m/s. Therefore, it can be concluded that a reduction in cell size decreases the yield stress of random honeycomb materials. Moreover, honeycombs with different irregularities exhibit consistent yield-surface responses under high-velocity impact, whereas honeycombs with the same cell size show closer agreement in their yield surfaces under low-velocity loading. These findings provide useful guidance for analyzing the yield surfaces of random honeycomb materials with different meso-structural parameters.

6 CONCLUSIONS

This study investigates the mechanical properties of random honeycomb materials under compression-shear combined loadings through experimental and numerical methods. A yield criterion was developed to predict the yield surfaces of random honeycombs under compression shear loadings. The following conclusions can be obtained:

(1) Quasi-static compression-shear combined loading tests showed that lower irregularity and greater cell-wall thickness increase both the normal and shear stresses of random honeycombs. In contrast, when the relative density is kept constant, a reduction in cell size decreases both the normal and shear stresses.

(2) Finite element simulations validated by dynamic drop-weight tests showed that the effects of the meso-structural parameters on the stress-strain curves are consistent with those observed under quasi-static loading. In addition, the influence of the strain-rate sensitivity of the base material depends on the deformation mode of the random honeycomb material.

(3) A yield criterion was established, and the corresponding yield surfaces were constructed. The results reveal that the normal yield stress is primarily affected by the loading velocity, whereas the shear yield stress is influenced by both the loading angle and the loading velocity.

Acknowledgments

Natural Science Foundation of Shaanxi Province (Grant No. 2021JQ-220).

Author's Contribuitions: Conceptualization, Y.Y. Gui and G. Luo; methodology, Y.Y. Gui, Y.Z Xiao and G. Luo; software, C.P. Chai and G. Luo; validation, Y.Y. Gui, F. Hu amd Z.Y. Li; formal analysis, Y.Z Xiao and G. Luo; investigation, Y.Y. Gui and G. Luo; resources, C.P. Chai and G. Luo; data curation, Y.Z Xiao, F. Hu and Z.Y. Li; writing—original draft preparation, Y.Y. Gui.; writing—review and editing, Y.Z Xiao and G. Luo; visualization, Y.Y. Gui, Y.Z Xiao and G. Luo; supervision, G. Luo and Y.S Chen; project administration, G. Luo and Y.S Chen; funding acquisition, G. Luo and Y.S Chen. All authors have read and agreed to the published version of the manuscript.

Data Availability statement: Research data is only available upon request.

Editor: Marcilio Alves.

References

San Ha N, Lu G., (2020). A review of recent research on bio-inspired structures and materials for energy absorption applications. Composites Part B: Engineering, 181, 107496.

Yin S, Wang H, Li J, et al., (2019). Light but tough bio-inherited materials: Luffa sponge based nickel-plated composites. Journal of the mechanical behavior of biomedical materials, 94, 10-18.

Zhang W, Yin S, Yu T X, et al., (2019). Crushing resistance and energy absorption of pomelo peel inspired hierarchical honeycomb. International Journal of Impact Engineering, 125, 163-172.

Rhee H, Tucker M T, Whittington W R, et al., (2015). Structure-property responses of bio-inspired synthetic foams at low and high strain rates. Science and Engineering of Composite Materials, 22(4), 365-373.

Qi C, Jiang F, Yang S., (2021). Advanced honeycomb designs for improving mechanical properties: A review. Composites Part B: Engineering, 227, 109393.

Liang H, Zhao Y, Chen S, et al., (2023). Review of Crashworthiness studies on cellular structures. Automotive Innovation, 6(3), 379-403.

Wang S. L., Zhang M., Wang Y., et al., (2021). Experimental studies on quasi-static axial crushing of additively-manufactured PLA random honeycomb-filled double circular tubes. Composite Structures, 261, 113553.

Du F., Zhou J. K., Tan T. et al., (2023). Mechanical Properties of Porous Metallic and Natural Foams. Comprehensive Structural Integrity, 10, 262-273.

ARCAN M., HASHIN Z. A., VOLOSHIN A, (1978). A method to produce uniform plane-stress states with applications to fiber-reinforced materials: a specially designed specimen yields material properties under pure shear or uniform plane-stress conditions. Experimental mechanics, 18. 141-6.

Doyoyo M., Wierzbicki T., (2003). Experimental studies on the yield behavior of ductile and brittle aluminum foams. International Journal of Plasticity, 19(8), 1195-214.

Zhao Z, Liu C, Wang H, et al., (2022). Crushing behavior of curved Nomex honeycombs under combined shear-compression loads. International Journal of Mechanical Sciences, 228, 107480.

Duan Y, Liu Z, Zhao X, et al., (2020). Crushing behavior of honeycomb vs. foam under combined shear-compression loading. Inter-national Journal of Impact Engineering, 146, 103696.

Tounsi R, Markiewicz E, Haugou G, et al., (2016). Dynamic behaviour of honeycombs under mixed shear-compression loading: Experiments and analysis of combined effects of loading angle and cells in-plane orientation. International Journal of Solids and Structures, 80, 501-511.

Zhang D, Lu G, Ruan D, et al., (2019). Quasi-static combined compression-shear crushing of honeycombs: An experimental study. Materials & Design, 167, 107632.

Abdulhameed O, Al-Ahmari A, Ameen W, et al., (2019). Additive manufacturing: Challenges, trends, and applications. Advances in Mechanical Engineering, 11(2), 1687814018822880.

Askari M, Hutchins D A, Thomas P J, et al., (2020). Additive manufacturing of metamaterials: A review. Additive Manufacturing 2020, 36, 101562.

Koju N, Niraula S, Fotovvati B., (2022). Additively manufactured porous Ti6Al4V for bone implants: a review. Metals, 12(4), 687.

Lv Y, Wang B, Liu G, et al., (2021). Metal material, properties and design methods of porous biomedical scaffolds for additive manufacturing: a review. Frontiers in Bioengineering and Biotechnology, 9, 641130.

Hong S.T., Pan J., Tyan T., et al., (2006). Quasi-static crush behavior of aluminum honeycomb specimens under compression dominant combined loads. International journal of Plasticity, 22(1), 73–109.

Hong S.T., Pan J., Tyan T., et al., (2006). Quasi-static crush behavior of aluminum honeycomb specimens under non-proportional compression-dominant combined loads. International journal of Plasticity 2006, 22(6), 1062–1088.

Mohr D., Doyoyo M., (2004). Experimental investigation on the plasticity of hexagonal aluminum honeycomb under multiaxial loading. Journal of Applide. Mechanics, 71(3), 375–385.

Hou B, Ono A, Abdennadher S, et al., (2011). Impact behavior of honeycombs under combined shear-compression. Part I: Experiments. International Journal of Solids and Structures, 48(5), 687-697.

Hou B., Pattofatto S., Li Y.L., et al., (2011). Impact behavior of honeycombs under combined shear-compression. Part II: analysis. International Journal of Solids and Structures, 48(5), 698–705.

Ashab A., Wong Y.C., Lu G., et al., (2013). Indentation tests of aluminium honeycombs s. Journal of Physics: Conference Series, Volume 451, International Symposium on Dynamic Deformation and Fracture of Advanced Materials (D2FAM 2013), Loughborough University, UK.

Ashab A., Ruan D, Lu G, et al., (2016). Finite element analysis of aluminum honeycombs subjected to dynamic indentation and compression loads. Materials, 9(3), 162.

Luo G., Mo D., Chai C., et al., (2023). Mechanical and Energy-Absorption Properties of a 3D-Printed Star-Shaped Auxetic Honeycomb under Combined Compression-Shear Loading. Latin American Journal of Solids and Structures, 20, 486.

Luo G., Chai C., Zhu Z., et al., (2024). Research on the Crashworthiness of 3D Printing Gradient Random Honeycomb Sandwich Structure and Multi-objective Optimization Design. Automotive Engineering, 46(11), 2110-2121.

Li K., Gao X.L., Wang J., (2007). Dynamic crushing behavior of honeycombs structures with irregular cell shapes and non-uniform cell wall thickness. International Journal of Solids and Structures, 44, 5003–5026.

Luo G., Chai C., Chen Y., et al., (2023). Investigations on the quasi-static/dynamic mechanical properties of 3D printed random honeycombs under in-plane compression. Thin-Walled Structures, 190, 110931.

Wang S., Wang H., Ding Y., et al., (2020). Crushing behavior and deformation mechanism of randomly honeycombs cylindrical shell structure. Thin-Walled Structures, 151, 106739.

ASTM Subcommittee D20. 10 on Mechanical Properties. Available online: astm.org/membership-participation/technical-committees/committee-d20/subcommittee-d20/jurisdiction-d2010 (accessed on 1st Nov. 2025).

Feng G. Z., Li S., Xiao L. J., et al., (2021). Energy absorption performance of honeycombs with curved cell walls under quasi-static compression. International Journal of Mechanical Sciences, 210, 106746.